THE FOG REMOTE SENSING AND MODELING FIELD PROJECT

BY I. GULTEPE, G. PEARSON, J. A. MILBRANDT, B. HANSEN, S. PLATNICK, P. TAYLOR, M. GORDON, J. P. OAKLEY, AND S. G. COBER

A field project that includes surface observations, remote sensing, and forecast models provides a better understanding of fog-induced low visibility and improves the parameterization of fog microphysics.

The total economic loss associated with the impact of fog on aviation, marine, and land transportation can be comparable to those of winter storms. For example, in the pre-Christmas period of 20–23 December 2006, the British Airport Authority (BAA) reported that a blanket of fog and freezing fog over the United Kingdom (UK) forced 175,000 passengers to miss flights from its seven British airports, with Heathrow being the worst affected (Milmo 2007). Early estimates suggested that this disruption to air travel cost British Airways at least £25 million (Gadher and Baird 2007). The costs to stranded passengers in terms of money and inconvenience may be impossible to calculate. Previous studies have also shown that human and financial losses due to accidents related to fog episodes are very common. In Canada, approximately 50 people per year die because of motor vehicle accidents (Gultepe et al. 2007a) in which fog was a contributing factor (Transport Canada Report 2001). In describing ground transportation in Illinois, Westcott (2007) stated that approximately 4,000 accidents and 30 deaths occur annually under foggy conditions in Illinois, excluding the city of Chicago. In Europe, a major fog project called Cooperation in Field of Scientific and Technical Research (COST-722), with objectives of reducing economic loss and fatalities, was also created to develop advanced methods for very short-range forecasts of fog and low clouds (Jacobs et al. 2007).

A dense fog event with low visibility values of about 50 m occurred on 27 Dec 2008. On this day, there was at least 15 cm snow on the ground in Toronto, Ontario, Canada when rain started at about 9:00 a.m. local time. The combination of rain falling and snow on the ground with temperatures reaching up to 10°C resulted in very dense fog in the boundary layer.

Petterssen (1956) suggested that fog classification based on temperature (T) can be divided into three types: 1) liquid fog ($T > -10$°C), 2) mixed phase fog (-10°C $> T > -30$°C), and 3) ice fog ($T < -30$°C). The criteria used in this respect do not always occur in a clear-cut fashion as implied by the classification. For example, ice fog may occur at $T = -10$°C, when excessive vapor is used by ice nuclei in a steady-state condition with no mixing processes. Freezing fog sometimes occurs when T gradually decreases below 0°C, and this is one of the common fog types in the northern latitudes.

Previous studies on fog forecasting/nowcasting suggested that a better understanding of fog microphysics and the large/small scale effects on its formation is needed to develop accurate forecasting models (Tardif 2007; Gultepe and Milbrandt 2007; Pagowski et al. 2004). Soil–atmosphere exchanges are also important for fog formation and dissipation. Fog forecasting/nowcasting is usually done using detailed one-dimensional (1D) boundary layer (BL) models that utilize initial boundary conditions obtained from 3D limited-area models (Guedalia and Bergot 1994; Bergot et al. 2005; Kunkel 1984) or from cloud and fog models (Gultepe and Milbrandt 2007; Bott 1991; Bott et al. 1990). Current parameterizations for fog visibility (Vis) in numerical models are not accurate (Gultepe et al. 2006a; Muller et al. 2007) because of the incomplete treatment of the physics and unresolved microphysical issues (Teixeira 1999), such as neglected droplet number concentration (N_d). Studies performed during COST-722 (Gultepe 2006a, Jacobs et al. 2007) showed that N_d should be included in visibility parameterizations; otherwise, the uncertainty in Vis can exceed 50%.

Satellite observations can be used for fog detection at nighttime when mid- and high-level clouds are not present because the 3.7-μm channel detects only the infrared (IR; Ellrod 1995) radiance as opposed to the sum of the shortwave (SW) and IR radiances during daytime. Therefore, a daytime fog algorithm needs to include the removal of SW contribution to the 3.7-μm channel. An integration of observations from surface-based sensors, remote sensors, and model data, as proposed by Gultepe et al. (2007b) for fog forecasting, might improve predictions/nowcasts for daytime applications. Ellrod and Gultepe (2007) also showed that integration of surface temperature observations with Geostationary Operational Environmental Satellite (GOES) observations can improve fog forecasting skill up to 20%. Recently, Bendix et al. (2006) used the Moderate Resolution Imaging Spectroradiometer (MODIS) data for fog remote sensing, and their results suggested that an increase in channel numbers in the near-IR region is useful for high-resolution fog retrievals.

To better evaluate forecasts of fog formation, development, and dissipation, field observations can be used for verification purposes. This can be done with 1) analyzed climatological surface data (Tardif and Rasmussen 2007), 2) in situ observations (Gultepe et al. 2006a,b, 2007b), and 3) remote sensing data (Cermak and Bendix 2007, 2008). Detailed studies by Tardif and Rasmussen (2007) and Hansen et al. (2007) suggest that climatological data can help in developing a better understanding of fog formation and forecasting methods, as well as organizing better field programs (Gultepe et al. 2006b).

Several field studies that focused on fog and other boundary layer clouds were performed over the last few decades. Among the regions where these experiments took place are the coastal regions off the California coast in the western United States. Review articles focused on West Coast marine fog and stratocumulus were presented by Leipper (1994) and Kloesel (1992). Another noteworthy experiment was the Cooperative Experimental in West Coast Oceanography and Meteorology (CEWCOM) project

AFFILIATIONS: Gultepe, Hansen, and Cober—Cloud Physics and Severe Weather Research Section, Meteorological Research Division, Science and Technology Branch, Environment Canada, Toronto, Ontario, Canada; Pearson—National Laboratory for Marine and Coastal Meteorology, Environment Canada, Dartmouth, Nova Scotia, Canada; Milbrandt—Numerical Weather Prediction Research Section, Meteorological Research Division, Science and Technology Branch, Environment Canada, Dorval, Quebec, Canada; Platnick—Laboratory for Atmospheres, NASA Goddard Space Flight Center, Greenbelt, Maryland; Taylor and Gordon—Department of Earth and Space Science and Engineering, York University, Toronto, Ontario, Canada; Oakley—School of Electrical and Electronic Engineering, University of Manchester, Manchester, United Kingdom
CORRESPONDING AUTHOR: Ismail Gultepe, Cloud Physics and Severe Weather Research Section, Meteorological Research Division, Science and Technology Branch, Environment Canada, Toronto, Ontario, M3H 5T4, Canada
E-mail: ismail.gultepe@ec.gc.ca

The abstract for this article can be found in this issue, following the table of contents.
DOI:10.1175/2008BAMS2354.1

In final form 26 August 2008

(Noonkester 1977), which consisted of a major set of experiments off the California coast conducted during 1972–82 under the U.S. Naval Air Systems Command. These series of meso- and micrometeorological experiments involved a land and sea network of radiosonde observations, ships, aircraft, balloons, and kites. Studies based on observations were complemented by modeling studies.

An investigation of low-level stratus/fog was performed by Koracin et al. (2001). Using a 1D model and observations, they stated that both radiative cooling and large-scale subsidence were important factors for fog formation. Radiation fog studies using detailed surface observations were led by Meyer and Lala (1986), Roach et al. (1976), Choularton et al. (1981), and Müller et al. (2007). These works also focused on various aspects of fog formation and its evolution using numerical models. Fuzzi et al. (1992) carried out the Po Valley Fog Experiment in northern Italy, which was a joint effort by several European research groups from five countries. The physical and chemical behavior of the multiphase fog system was studied experimentally by following the temporal evolution of the relevant chemical species in the different phases (gas, droplet, interstitial aerosol) and microphysical conditions during fog formation, evolution, and dissipation periods. Fuzzi et al. (1998) also conducted a second field project called Chemical Composition of Droplets (CHEMDROP) that took place in the Po Valley region. Their project focused mostly on fog microphysics and chemistry, as in the previous field experiment.

SCIENTIFIC OBJECTIVES. The main purpose of this paper is to describe the Fog Remote Sensing And Modeling (FRAM) project and to summarize the preliminary results. The overall objectives of FRAM are to

1) characterize fog formation, evolution, and dissipation in continental and marine environments;
2) parameterize the fog microphysics for numerical weather prediction model applications;
3) improve the numerical model simulations and remote sensing applications;
4) improve and understand instrument capabilities for detection of fog and fog environments and measurements of associated microphysical parameters; and
5) integrate observational and model data to improve uncertainties in fog forecasting/nowcasting.

These objectives will be accomplished using various observations and numerical methods described here.

The next section summarizes the project sites and instruments used for data collection. A section on visibility concepts follows. The preliminary results section focuses on warm and ice fog cases that were observed and includes a summary of observations and climatologies of the project areas. This is followed by the summary and conclusions.

PROJECT SITE AND INSTRUMENTS. Three field campaigns of the FRAM project were conducted over the following two regions of Canada: 1) the Center for Atmospheric Research Experiments (CARE) near Egbert, Ontario (FRAM-C), which represented continental fog environments, and 2) Lunenburg, Nova Scotia (FRAM-L), which represented marine fog environments. FRAM-C took place during the period from November 2005 to April 2006, and FRAM-L1 and L2 occurred during June 2006 and June 2007, respectively. The FRAM-L2 project was performed to compare the statistics on the occurrence of fog and instrument performance over the same area for two subsequent years. The locations for FRAM sites were chosen based on a 30-yr fog climatology of the related sites. A detailed fog climatology study over Canada is in progress and can be found in Hansen et al. (2007).

Several instruments were deployed during the field campaigns (Table 1). Observations from these instruments were collected at 1-Hz sampling rate, excluding turbulence measurements collected at 32 Hz. Pictures of some instruments are shown in Fig. 1, including the Droplet Measurement Technology (DMT) fog measuring device (FMD; FM-100), Climatronics Aerosol Profiler (CAP), Vaisala ceilometer (CT25K), York University ice particle counters (IPC; Savelyev et al. 2006; Brown and Pomeroy 1989), total precipitation sensor (TPS), Particle Measuring System (PMS) Forward Scattering Spectrometer Probe (FSSP), PMS Particle Cavity Axial Spectrometer Probe (PCASP), Radiometrics Profiling Microwave Radiometer (PMWR), and Vaisala all-weather sensor (FD12P). Observations collected included droplet, ice particle and aerosol sizes and number concentrations from optical probes, visibility from a Vaisala visibility sensor, liquid water content (LWC), relative humidity with respect to water (RH_w), T, and liquid water path (LWP) from a PMWR. The fog coverage and some microphysical parameters (e.g., droplet size, phase, and LWP) were also obtained from GOES and MODIS products.

A new instrument called ClearView (DMIST, Inc., Manchester, United Kingdom, online at www.dmist.com) was used to calculate the visibility from the

Table 1. The list of surface instruments that were available during FRAM projects. The LWC, LWP, N_d, T, q_v, and RH_w represent the liquid water content, liquid water path, droplet number concentration, temperature, vapor mixing ratio, and relative humidity with respect to water, respectively. The C and L after FRAM represent the CARE and Lunenburg sites, respectively. The FMD and TPS are for fog measuring device and total precipitation sensor, respectively.

Instrument	FRAM-C	FRAM-L1/L2	Measurement	Measurement range
FMD (SPP-FM DMT Inc.)	x	x/x	Droplet size, LWC, N_d	1–50 μm
FSSP	x	—	Droplet size, LWC, N_d	1–48 μm
PCASP	x	—	Aerosol size, mass, concentration	0.1–3 μm
YES TPS (hot plate)	x	—	Precipitation rate	>0.1 mm h^{-1}
DMT CIP (cloud imaging probe)	—	–/x	Size, LWC, N_d, for ice and droplets	15–1550 μm
YU ice particle counters (IPC)	x	—	Number concentration and particle flux	>50 μm and <2 mm
MWR1100	x	—	LWP, T, vapor mixing ratio (q_v)	>0.05 g m^{-2}
MWR TP3000	x	x/–	LWC, T, q_v	>0.05 g m^{-2}
Vaisala FD12P	x	x/x	Visibility, precipitation type, intensity	>0.1 mm h^{-1}
Vaisala VRG101	—	–/x	Precipitation intensity and amount	>0.2 mm h^{-1}
Vaisala ceilometer CT25K	x	x/x	Cloud-base height and backscatter profile	—
POSS	x	—	Precipitation type and intensity	—
Climatronic aerosol profiler (CAP)	—	x/x	Aerosol size and concentration	0.3–10 μm; 8 channels
ClearView video unit	—	x/x	Images and visibility	—
Young sonic anemometer [81000]	—	x/x	3D wind speed and turbulence	4–32-Hz sampling rate
Vaisala DST111	—	–/x	Surface T measurement	−50 to +50°C
Vaisala DSC111	—	–/x	Water amount	10 mm
Eppley IR; SW radiometers	x	x/x	Broadband radiative fluxes	5%–10% uncertainty
Buoys	—	x/x	T, RH, wind	1-Hz sampling rate
Wind profiler RASS	x	–/x	T, wind, fog boundaries	1-min averages
Campbell Scientific HMP45C	x	x/x	T and RH	±1°C; 5%

images taken by a digital video camera. A common atmospheric degradation seen in images is additional lightness resulting from optical scattering; the effect has been called "airlight" (Oakley and Satherley 1998). The airlight leads to an additive offset that is accompanied by attenuation of the scene content resulting from scattering. Taken together, these factors lead to a loss of contrast and color in the image. With a forward-looking camera, the optical depth is greater in the upper part of the image and so the contrast decreases progressively with image height.

The total number of cases with Vis < 1 km during FRAM-C was 19. During FRAM-L1 and FRAM-L2, the total number of cases with Vis < 1 km was 27 and 10, respectively. During FRAM-L2, some additional instruments (Table 1) were used. For example, surface soil temperature and surface state (e.g., water amount) measurements were only available during FRAM-L2. These additional measurements can be useful to indicate the availability of the moisture at the surface just prior to fog formation.

VISIBILITY CONCEPT. The following instruments were used to obtain visibility: 1) FD12P (Gultepe and Isaac 2006), 2) DMIST ClearView (Oakley and Satherley 1998), and 3) FMD (Gultepe and Milbrandt 2007). Visibility calculations used for these instruments were based on the extinction of visible light. Using the particle spectra measured by FMD, Vis is obtained using the following formula,

where the extinction coefficient is obtained using the Mie theory for droplets:

$$\beta_{ext} = \sum Q_{ext}(r, \lambda) n(r) \pi r^2 \Delta r, \quad (1)$$

where n is the number density of particles in a bin size of radius (r) and Q_{ext} is the extinction efficiency related to r and the wavelength (λ) of visible light. When the droplet size increases to larger than about 4 μm, the value of Q_{ext} reaches approximately 2. The Q_{ext} fluctuates between 3.8 and 0.9 for particle sizes less than 4 μm. The extinction parameter is converted to Vis following Stoelinga and Warner (1999) as

$$\text{Vis} = -\ln(0.05)/\beta_{ext}, \quad (2)$$

where 0.05 represents a threshold for brightness contrast. The FD12P provides the meteorological observing range (MOR) that is based on the contrast threshold of 0.05. To show a relationship between Vis and ice crystal number concentration (N_i) for ice fog, Vis from the FD12P is plotted against IPC measurements (Brown and Pomeroy 1989), where wind speed was significantly smaller (2–3 m s^{-1}) than blowing snow conditions (>7 m s^{-1}; Gordon et al. 2006). The following equations are used for calculations of the ice particle number flux and ice fog number concentrations:

$$N_{if} = C/A \quad \text{and} \quad N_i = C/AU_w, \quad (3)$$

where C is the average number of particles per second crossing the transmitted beam (Hz), A is the beam cross-section area (m^2), and N_{if} and N_i are the ice particle number flux (m^{-2} s^{-1}) and ice crystal number concentration (m^{-3}), respectively. The variable U_w is the horizontal wind speed measured at the 10-m level. The A values for IPC1 (at 0.7 m) and IPC2 (at 2.5 m) were 6.15×10^{-6} m^2 and 5.85×10^{-6} m^2, respectively. In N_i calculations, it was assumed that U_w at 10 m was also representative of winds at approximately 2 m, because ice fog conditions occurred during calm wind conditions (<0.5 m s^{-1}). Ice fog visibility (Gultepe and Isaac 2006) can then be parameterized by searching for a relationship between N_i and Vis. In N_i–Vis parameterization, unknown particle shape and number concentration for ice crystal sizes less than 50 μm can result in large uncertainties in extinction (also visibility) calculations. Gultepe et al. (2008) showed that ice crystal particles sizes in a typical ice fog event occurred in April of 2008 in Barrow, Alaska, during the Indirect and Semi-Direct Aerosol Campaign (ISDAC) project (Gultepe et al. 2008) were less than 20 μm and that their concentration reached up to 10–100 cm^{-3}. Usually, N_i within the clouds can be a few counts per liter (<100 l^{-1}) for sizes greater than 50–100 μm. In addition to N_i, accurate ice water content (IWC) measurements are needed to obtain better Vis parameterizations (Gultepe et al., 2008).

PRELIMINARY RESULTS. *Climatology of FRAM project areas from 1970 to 2004.* The locations of the FRAM field campaigns at Egbert, Ontario, and Lunenburg, Nova Scotia, were sufficiently near Toronto, Ontario, and Shearwater, Nova Scotia, respectively, that the climatologies for the latter stations should be similar in nature. The climatology (1970–2004) of both the Toronto Pearson International Airport in Ontario and Shearwater in Nova Scotia are shown in Figs. 2a,b, respectively. Following the World Meteorological Organization (WMO) definition, fog over a 30-yr period was assessed when Vis

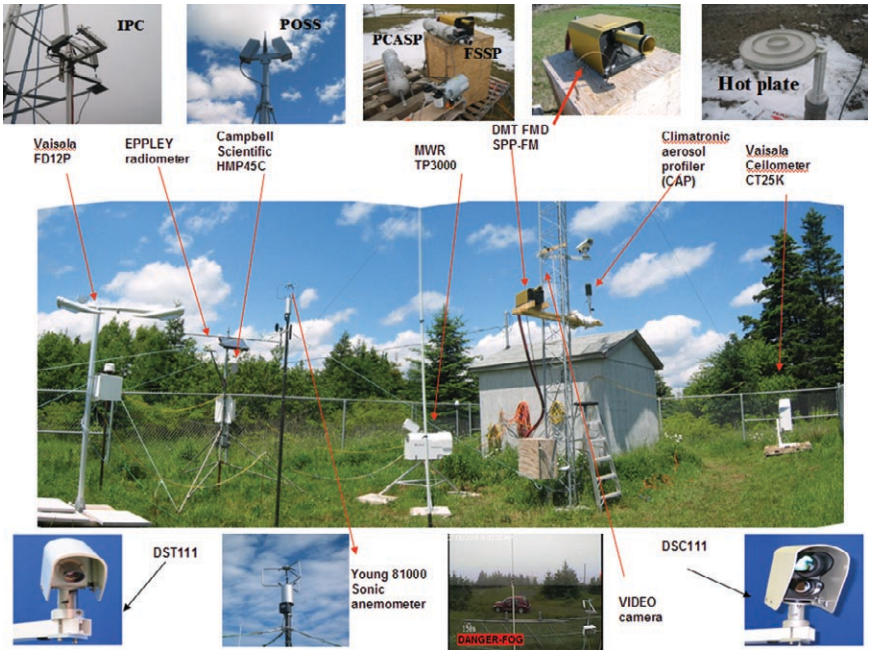

Fig. 1. Instruments deployed during FRAM-C and FRAM-L phases of the fog project. Additional information can be found in Table 1.

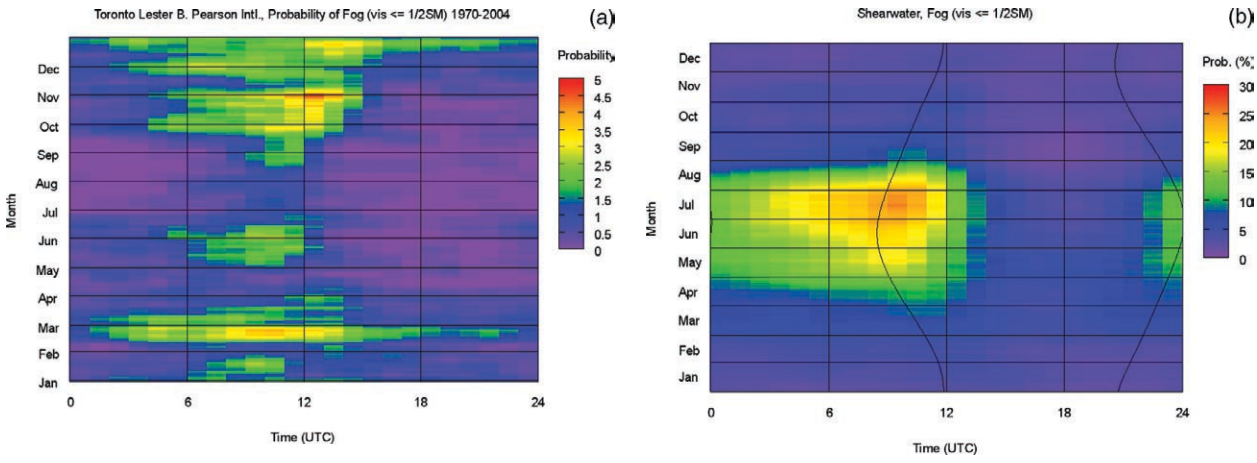

Fig. 2. Fog climatology of (a) Toronto Pearson International Airport, Ontario, and (b) Shearwater, Nova Scotia. The time period covers from 1970 to 2004 with Vis < 1 km. The y axis shows the day and month of the year and the *x* axis shows the time of day. The color bar shows the probability of fog occurrence.

in the horizontal becomes less than 1 km. Figure 2a shows that a high frequency of fog formation (up to 5%) at Pearson Airport with Vis less than 1 km occurs during the months of October and March. The fog frequency reaches up to 30% of the time during May–August for Shearwater (Fig. 2b). The fog occurrence from both FRAM-C and FRAM-L1 (L2) projects are found to be ~16% and ~77% (33%) of time, respectively (e.g., Vis < 1 km and lasted more than 15 min). The results obtained during the field campaign measurements showed that fog occurrence for both the Ontario and Nova Scotia regions were much higher than those used in the fog climatology that were based on traditional human observations (Fig. 2). This result is also likely to be affected by 1) the coast near Lunenburg, which is probably foggier than Shearwater in general, and 2) the fog occurrence for any given month that may vary significantly from the 30-yr climatology. In addition, the field campaign programs were of a relatively short duration and may not be representative of the local climatology.

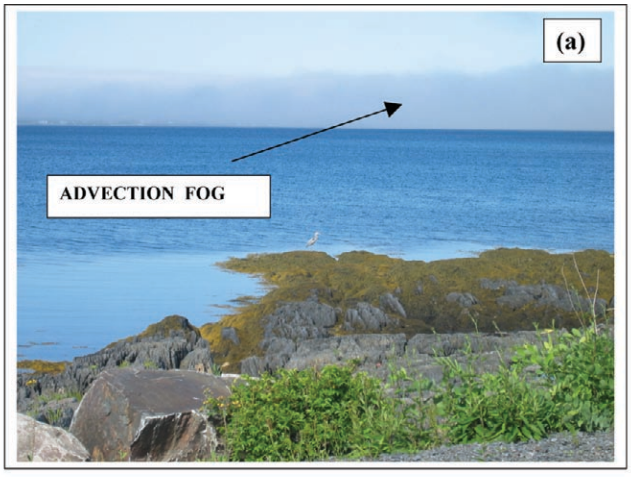

Fig. 3. An example marine fog case: (a) picture taken at 1430 EST on the 27 June 2006 and (b) time series of RH_w, visibility averaged over 1-min and 10-min intervals (Vis), temperature (T), and precipitation rate (PR).

27 June 2006 marine fog case. Advection of warm and moist air over the Atlantic Ocean from south of the project area on 27 June 2006 resulted in low Vis values, excluding the time period between 1000 and 1800 EST. Figure 3a shows a picture taken at 1430 EST. The fog layer moved back over the ocean during the daytime when the sun warmed the land and winds were diminished. Visibility obtained from the FD12P, together with other observations, is shown in Fig. 3b. The Vis was less than 0.5 km from midnight to early morning (0900 EST). After 1800 EST, fog

moved in again with Vis less than a few hundred meters. There was no significant rain and T was approximately 15°C with RH_w ~100%. The incoming SW broadband radiative fluxes (SWi) obtained using the Eppley Pyrgeometer instrument for a clear-air case on 17 June, plus another 11 days from FRAM-L1, are shown in Fig. 4. The SWi in the 27 June case decreased from ~400 (in clear air) to ~100 W m^{-2} (in foggy air) from about 0830 to 0930 EST. When both rain and fog were present as in the 15 June case, SWi became much smaller compared to the 27 June only-fog case. Using ~300 W m^{-2} decrease in SWi in the 17 June case in a fog layer of 1 km over a 1-h time period, the SW cooling is estimated at −9°C h^{-1}.

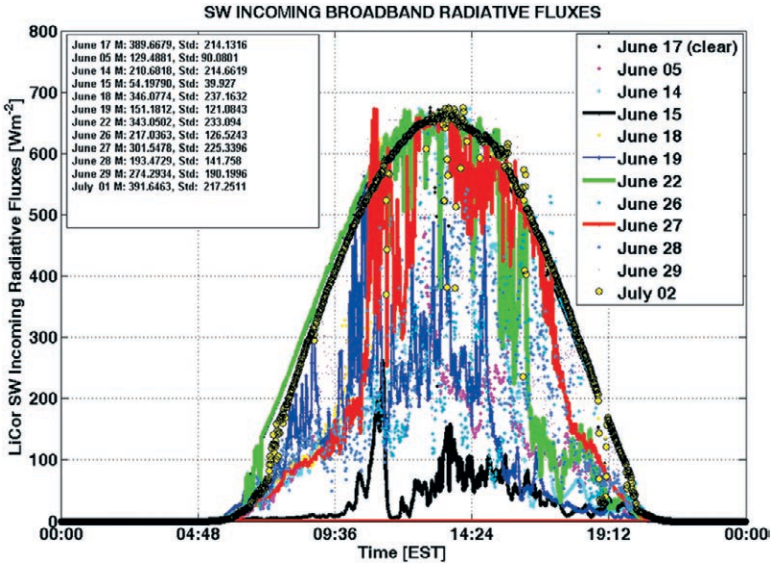

Fig. 4. Shows incoming SW broadband radiative fluxes versus time for various days during FRAM-L1. The data points for the 17 June and 2 July 2006 represent clear air conditions. Others represent either foggy (e.g., 19 June) or foggy plus rainy conditions (e.g., 15 June). The days with lines are for foggy conditions except for the 15 June 2006 case. Mean and standard deviation for entire day for each case are also shown on the figure.

The analysis of observations from the ClearView instrument suggested that Vis during this day changed from ~150 m in the early morning (Fig. 5a) to approximately 3 km at noontime (Fig. 5b). Both images have the corresponding Vis values overlaid in the bottom left corners.

GOES satellite observations were collected during FRAM. A fog algorithm (Gultepe et al. 2007b), based on integrating GOES and the Canadian Global Multiscale Model (GEM) numerical weather prediction (NWP) model output (Côté et al. 1998), was used for fog detection during the field project. MODIS operational cloud products (Platnick et al. 2003) were also available from the online Collection 5 data distribution site (http://ladsweb.nascom.nasa.gov). Figures 6a,b were generated from MODIS *Terra* data. Figure 6a is a false color RGB image of the foggy area. Figure 6b shows retrieved effective radius (R_{eff} between 7 and 15 μm along the shoreline of the project area). The R_{eff} is retrieved using a band combination that includes the MODIS 2.1-μm band (Platnick et al. 2003); R_{eff} retrievals using the MODIS 3.7-μm band are several microns smaller than observed values at the ground site and generally not larger than 15 μm in the southern cloud field; this is perhaps indicative

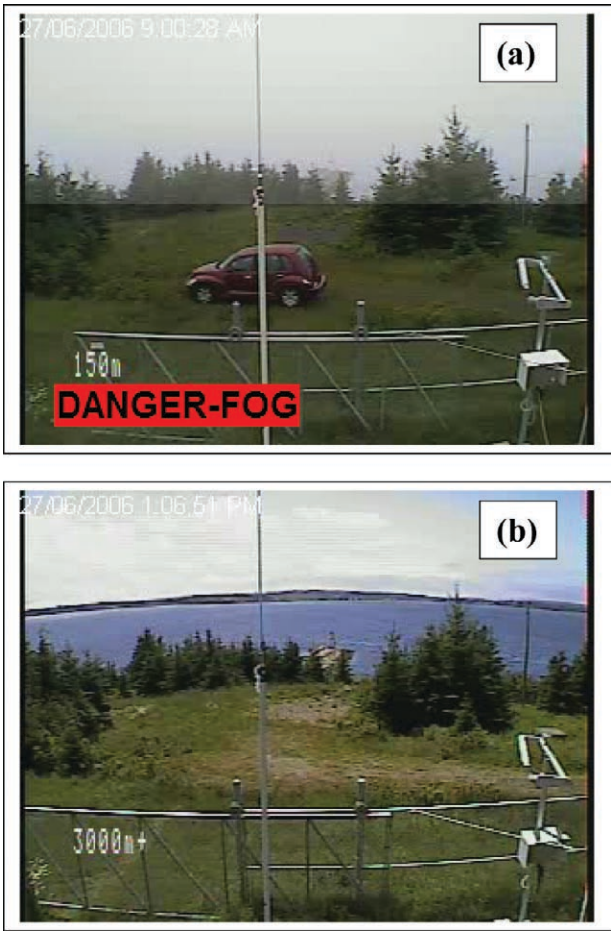

Fig. 5. The ClearView images for (a) the foggy conditions at 0900 EST (150 m) and (b) after fog dissipated (Vis = 3000 m) at 0107 EST on the 27 June 2006. When Vis becomes less than 1 km, Danger-Fog tag is seen on the image during the operations.

of microphysical vertical structure in the fog deck (Platnick 2000; Chang and Li 2003). Figure 6c shows the R_{eff} versus LWC obtained from the FMD measurements, where the median value of R_{eff} is about 7 μm over an approximately 6-h period (0300–0900 EST). Some significant differences between R_{eff} values of FMD and the MODIS *Terra* overpass (at 1035 EST) occurred because during the overpass the fog had receded form the ground site and lifted.

The time–height cross sections of T, RH_w, and LWC from the PMWR, TP3000 are shown in Figs. 7a–c, respectively, whereas the MODIS image was taken at 1435 EST when the fog retreated toward the ocean. Figure 7a shows that T ~16°C when RH_w ~100% during the fog event. The fog layer was below the 350-m level and had LWC ~0.3 g m^{-3}. The fog layer dissipated during the middle of the day when T reached ~23°C. The RH_w was about 70% above the fog layer and no higher-level clouds were observed during the fog episode, although some stratus developed during the fog dissipation. LWC retrievals from the PMWR, which uses integrated liquid water path and a fuzzy logic algorithm, can be useful for measuring fog properties. However, the LWC estimate may have a large uncertainty because the adiabatic assumption used is not correct for fog conditions unless the fog forms because of air rising over terrain. In addition, the thickness of the fog layer is usually less than a few hundred meters, which cannot be resolved using a statistical analysis method.

Time series of the 1-s N_d data from the FMD show that max N_d reached up to 300 cm^{-3} (Fig. 8a) and Vis corresponding to that value was about 300 m (Fig. 8b). The graph shows that increasing N_d results in lower Vis values. Bimodal size distributions were seen in the FMD droplet spectra for many cases (an example is shown in Fig. 8c). The separation at about 15 μm into two modes (at ~3 and 25 μm) was likely due to the presence of drizzle size droplets with sizes >15 μm in diameter. The FMD measurements were used to obtain a relationship between Vis and N_d and LWC. During the analysis, it was found that LWC increases with increasing N_d (not shown) and that the Vis decreases with increasing LWC and N_d, which are shown in Figs. 9a,b, respectively. Using 1-s measurements of LWC and N_d from the FMD, the fog settling rate (F_{sr}) as a function of both LWC and N_d, and the Vis versus 1/(LWC N_d) are shown in Figs. 9c,d, respectively. These figures suggest that Vis and F_{sr} parameterizations should include both LWC and N_d.

There have been some studies that use reflectivity obtained from the millimeter-cloud radars (e.g., λ = 8.6, 3.2, 2.14, and 1.36 mm) for fog detection (Mead et al. 1989; Wolf et al. 1999; Hamazu et al.

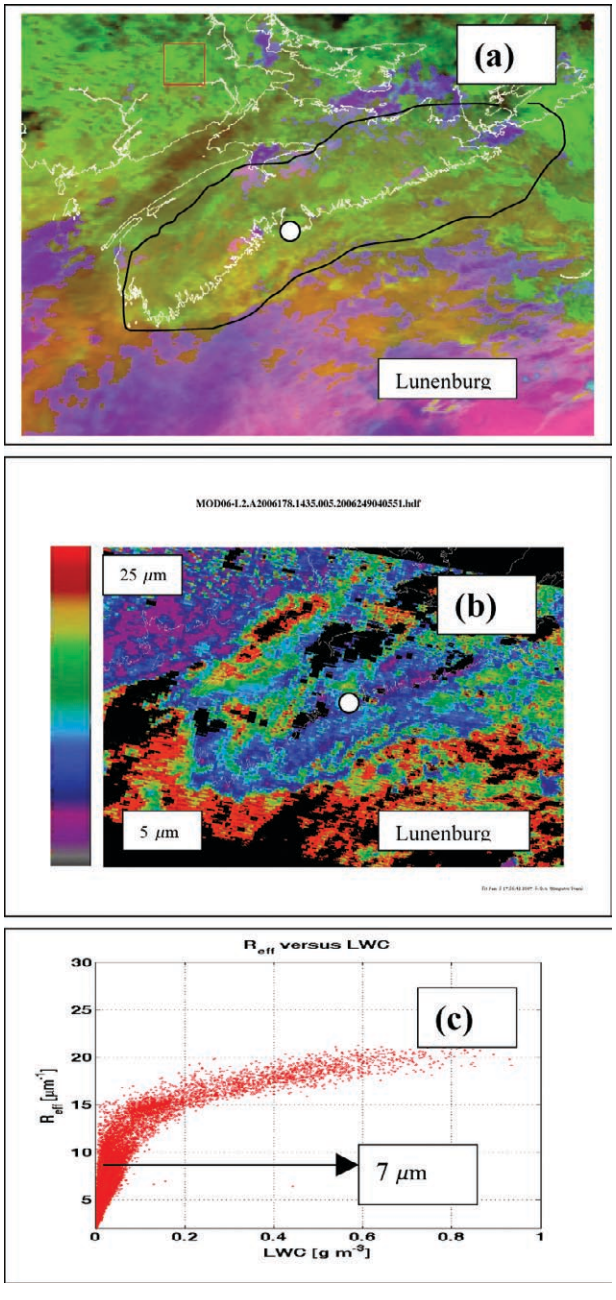

FIG. 6. MODIS false color RGB image (bands 11, 20, and 31) at 1035 EST for the 27 June 2006, during an intense fog event (a) where the foggy area is shown with a black line. The effective cloud particle size from the MODIS TERRA retrievals is shown in (b). The retrieved fog droplet effective sizes in the vicinity of the ground site are between 7 and 15 μm. Large R_{eff} further south of the coast are associated with small cloud optical thickness and large R_{eff} retrieval uncertainty (neither data product shown). The black regions represent the areas with no retrievals. R_{eff} versus LWC from the FMD is shown in (c). The median R_{eff} is found to be 7 μm.

2003; Uematsu et al. 2005). Because of a large variability in fog particle spectra as in the present study, the relationship between the radar reflectivity and the cloud microphysical parameters needs to be researched. Mead et al. (1989) suggested that relationships between the radar reflectivity factor and LWC can significantly be affected by mode radius. Hamazu et al. (2003) showed that the minimum detectable reflectivity factor (Z) for a millimeter radar in a fog study changed from −40 dBZ at 2-km range to −10 dBZ at 20-km range along the 500-m height level. Measurements of the FMD collected during FRAM-L are used in obtaining Z in Figs. 10a,b, which show Z versus LWC R^2_{eff}, and Vis versus Z, respectively. These results suggest that knowing Z from a millimeter radar, and assuming a constant R_{eff}, both fog LWC and Vis can be estimated from Z.

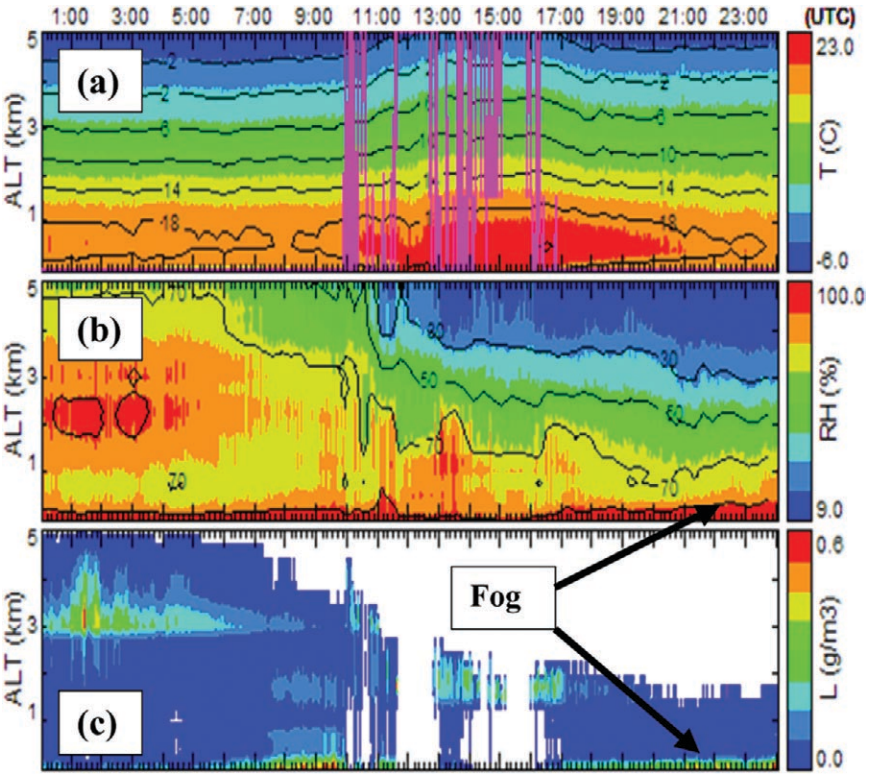

FIG. 7. (a) Time–height cross section of temperature (T), (b) RH_w, and (c) liquid water content (L) obtained from PMWR. The time is shown at the top panel. The pink color at the top panel is for cloud base height.

During FRAM, the FMD and CAP were used in obtaining particle characteristics of N_d and N_a, respectively. The first instrument consisted of 20 channels from 1 to 50 μm, while the second consisted of 8 channels from 0.3 to larger than 10 μm. When high RH_w exists, it is likely that the CAP measures both deliquesced aerosols and droplets. The combination of measurements from these instruments can help to integrate the spectra from sizes less than 1 up to 50 μm, although the FMD starts at about 2 μm. Figure 11, representing 1-s observations, shows the N_d and N_a spectra for 27 June (fog case) and 30 June (no fog case). When fog occurs, the FMD and CAP concentrations were found to be similar for sizes >2 μm, but the CAP measurements can significantly affect the Vis calculations when particles with sizes <1 μm are included. In cases without fog conditions, the CAP values were found to be significantly less than that of the FMD for fog cases for a given size, suggesting that when the winds were from the south, representing the ocean surface BL, cloud condensation nuclei (CCN) increased significantly and resulted in larger N_d. This can only be clarified with detailed measurements of the sizes and images of the small droplets.

Fog formation is usually considered a light-wind atmospheric phenomenon, but this is not true for the coastal environments where winds transport CCN together with warm and moist air from ocean surface to land. The Young ultrasonic instrument was used for obtaining the mean wind and 3D wind fluctuations (w_x', w_y', w_z') over 5-min periods. Turbulent kinetic energy (TKE) was then calculated using the fluctuations just before the fog started to move in (1800 EST) and after the fog completely moved in (2200 EST). Figures 12a–c show measured 32-Hz wind speed, fluctuations, and TKE for 1800 EST, respectively, while Figs. 12d–f show the same parameters but for 2200 EST. The higher turbulent fluctuations (w_z'= 4 m s^{-1}; TKE ~6 m^2 s^{-2}) with stronger southerly winds (~5 m s^{-1}) at 1800 EST caused the increased fog water content in the later time period. This likely happened due to increased moisture, availability of higher-condensation nuclei concentration, and mixing of cold and dry air above with moist and warm air below. When the boundary layer mass content became well mixed, turbulent fluctuations

(w_z' = 1 m s^{-1}; TKE < 2 m^2 s^{-2}) started to dissipate and the fog event lasted approximately another 12 h.

23 January and 10 February 2006 ice fog cases. Two ice fog cases were seen during the winter of 2005/06 at the CARE site. Unfortunately, the IPC was not available before 23 January 2006 and data were limited on that day; therefore, examples of the data from both 23 January and 10 February 2006 are presented here. Figure 13a (taken at 1000 EST) shows the leftover ice fog layer that occurred during the night of 23 January, between 0930 and 1430 EST. Figure 13b shows surface observations together with Vis obtained from the FD12P. The RH_w was about 95% and Vis ~100 m during the fog episode, and the FMD did not count any particles, suggesting that fog was patchy and variable in the area. The subsequent appearance of blue sky suggests that radiative cooling likely played an important role in the ice fog formation. During the ice fog episode, T was approximately −4° to −6°C and lasted for about 5 h. Ice fog can affect the radiative fluxes, resulting in radiative warming/cooling, depending on the microphysics of the fog. Ice fog studies (Bowling et al. 1968; Girard and Blanchet 2001; Gotaas and Benson 1965) were limited because of the difficulties in measurement of ice particles at sizes less than 100 μm (Gultepe et al. 2001), and this is still the case for current measurements.

The observations related to ice fog for the 10 February 2006 case are shown in Fig. 14. Figure 14a shows the time series of wind speed (U_w), indicating that usually it was less than 3 m s^{-1}. A max N_{if} (ice particle flux) of 0.08 × 10^6 m^{-2} s^{-1} (Fig. 14b) corresponds to a low Vis value in the time interval between 700 and 1200 min (Fig. 14c). Using the corresponding Vaisala measurements, the Vis values are plotted against N_i [obtained from Eq. (4)] as shown in Fig. 14d. The best fit regression line for the data shows that N_i ranges from 0.8 up to 50 L^{-1}. The Vis values are between 1 and 2 and 50 km, depending on N_i. As a simple estimate of expected N_i, assuming a particle radius of 5 μm (Ohtake and Huffman 1969) and Q_{ext} = 2, and using Eqs. (1) and (2) with Vis = 10 km, N_i then becomes 2550 L^{-1}, which is much higher than the number counted by the IPC (Huang et al. 2007). Using the particle radius set to 50 μm (as we assume for blowing snow), N_i = 26 L^{-1}. Evidently, the IPC cannot detect ice fog completely. It would be advantageous to modify the optical and electronic system to count smaller particles to obtain accurate values of Vis.

3D model simulation. A simulation was performed using the Canadian Mesoscale Compressible Community (MC2) model to illustrate the feasibility of explicitly forecasting Vis using an NWP model. The MC2,

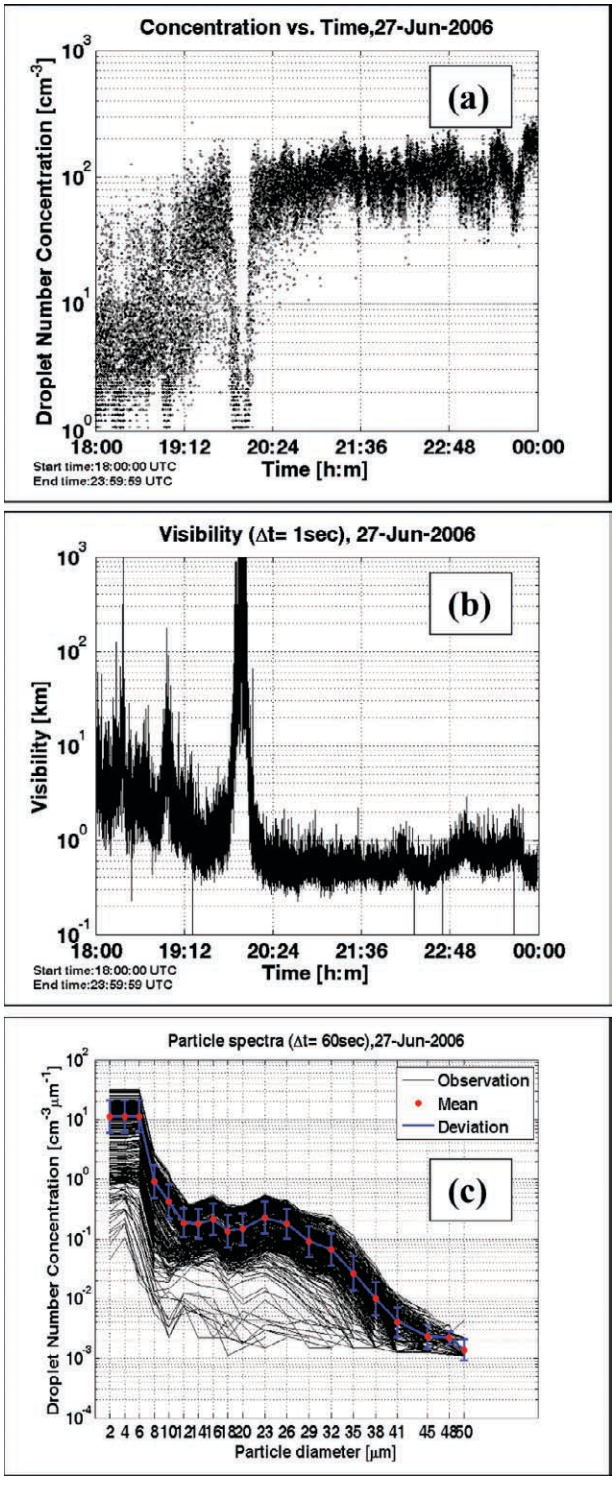

FIG. 8. Time series of (a) N_d, (b) Vis, and (c) particle spectra. (c) Midpoints for each spectral bin are shown as red filled circles, and standard deviations are shown as vertical bars with blue color.

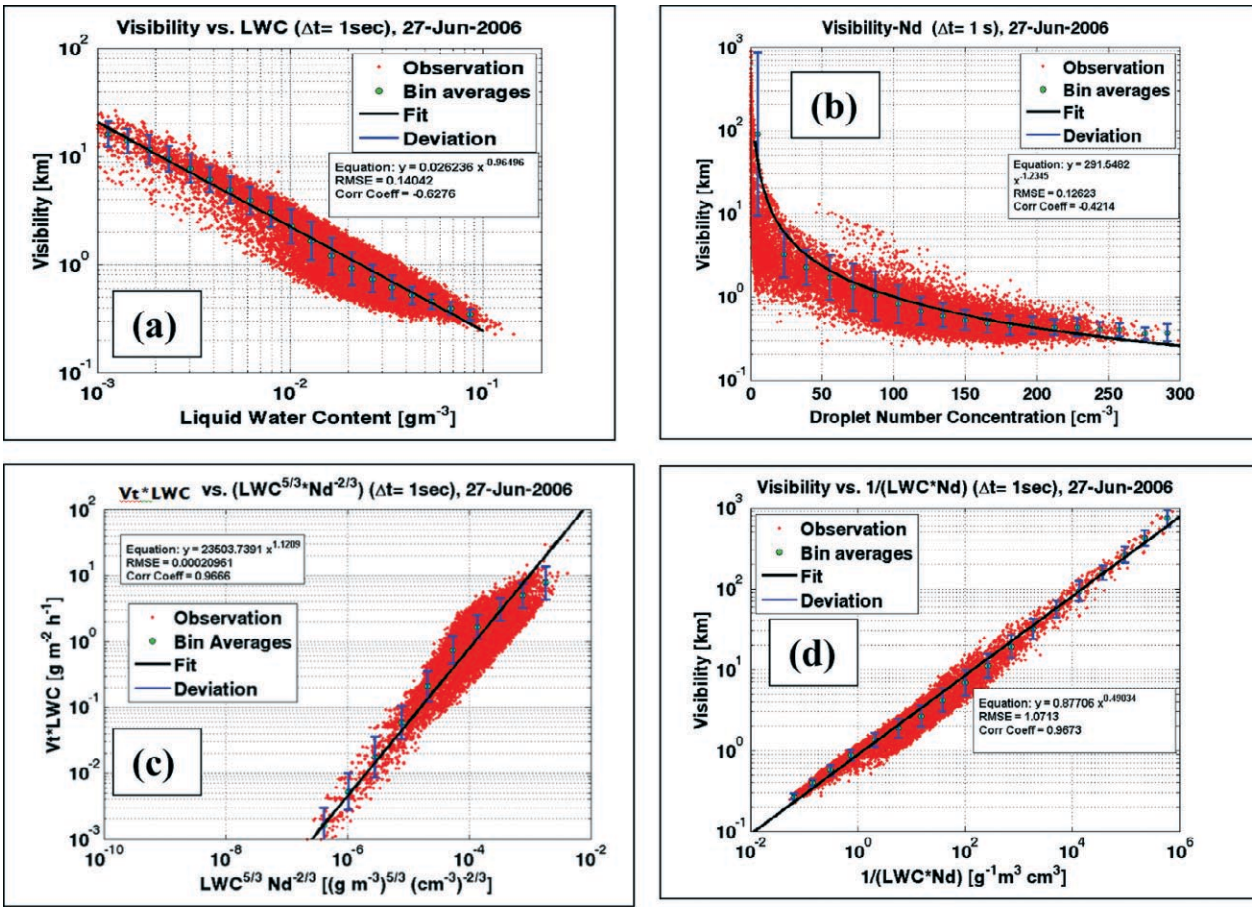

FIG. 9. Microphysical parameterizations based on 1-second observations: (a) Vis versus LWC, (b) Vis versus N_d, (c) the fog settling rate versus a function of LWC and N_d, and (d) Vis versus 1/(LWC*N_d). The fits are shown as straight lines and standard deviation is shown with bars. The fit relationships are shown over the figures.

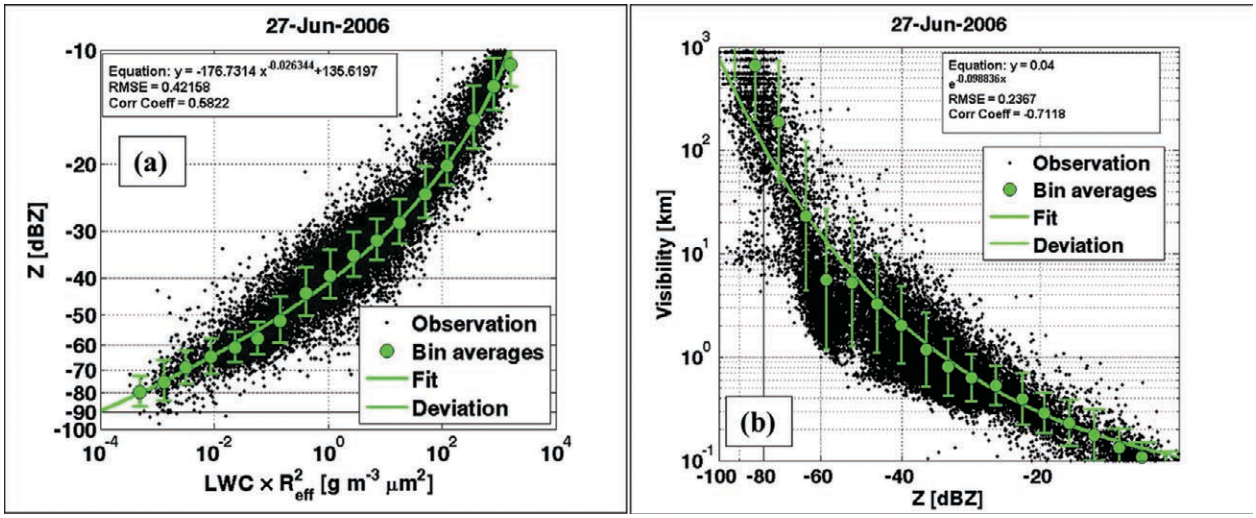

FIG. 10. (a) The reflectivity factor (Z) versus f(LWC;R_{eff}), and (b) Vis versus Z. The fit is shown over the 1-second observations together with standard deviations. The fit equations are also shown over each panel.

based on the fully compressible Euler equations, is solved on a Mercator projection; it is a limited-area model capable of one-way self-nesting. The model dynamics are discussed in detail in Benoit et al. (1997) and Thomas et al. (1998). The MC2 uses a comprehensive physics package (Mailhot et al. 1998), which

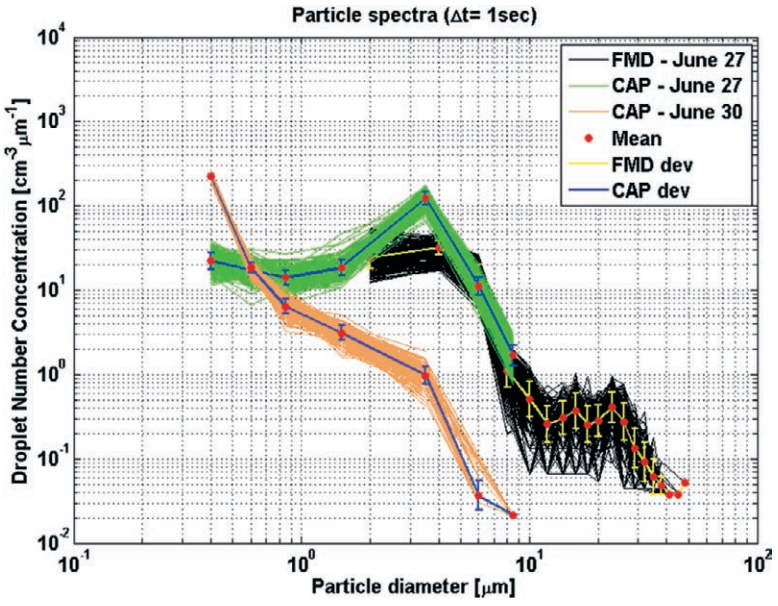

FIG. 11 (TOP). The CAP aerosol spectra overlaid on N_d spectra from the FMD for 1-second observations. The black lines are for N_d from the FMD and green lines for the CAP during the fog event on 27 June 2006.

FIG. 12 (BOTTOM). Wind components measured by the Young ultrasonic anemometer at 32 Hz for 5-min time interval at the start of fog event (1800 EST) on 27 June 2006 in panel (a). The mean and std dev values are also shown. The fluctuations are shown in panel (b). Mean and std dev for positive and negative wind fluctuations are also shown in panel (b). The turbulent kinetic energy (TKE) for the same time interval is shown in panel (c). Similar parameters are also shown in panels (d), (e), and (f) for 5-min time period, starting at 2200 EST for the same day where the fog developed into a mature state and the boundary layer became well mixed.

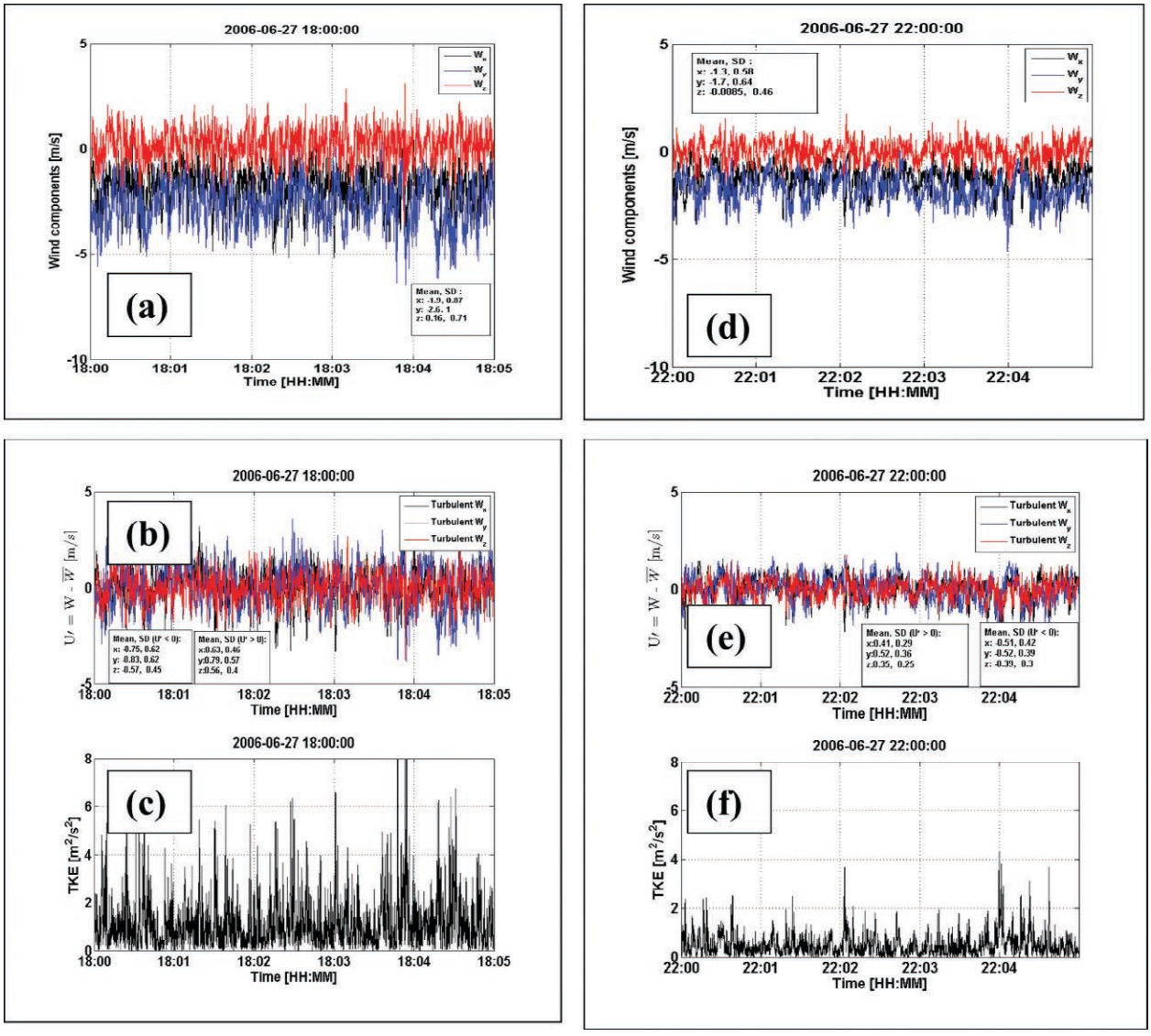

includes a planetary boundary layer scheme based on a turbulent kinetic energy concept (Benoit et al. 1989), implicit and explicit diffusion processes, and a detailed land-surface scheme (Bélair et al. 2003a,b). The solar (Fouquart and Bonnel 1980) and infrared (Garand and Mailhot 1990) radiation schemes used in model simulations are fully interactive with the model cloud microphysics.

Using a new Vis parameterization (Gultepe et al. 2006a) based on the N_d and LWC, Gultepe and Milbrandt (2007) applied the MC2 with prognostic equations for N_d and LWC for the 4 January 2006 fog event from the FRAM-C. On this day, a warm front moved across the Ontario region. The model was initialized on a coarse-resolution domain (10-km grid spacing; 301 × 301 points) using the 15-km regional analysis from the Canadian Meteorological Centre (CMC) for 0000 UTC 4 January 2006. Lateral boundary conditions from the CMC analyses were supplied every 6 h for a 24-h simulation. Using the output from the 10-km simulation, the model was then nested to a high-resolution domain (2-km grid spacing, 251 × 251 points) for an 18-h simulation, starting at 0600 UTC, 6 h after the initial time of the 10-km run. The purpose of this nesting strategy was to generate initial conditions for the 2-km simulation to reduce the model spinup time. Both simulations had 41 modified Gal-Chen levels (unevenly spaced) with 12 levels in the planetary boundary layer. The 10-km run employed a grid-scale condensation scheme similar to that of Sundqvist et al. (1989).

The 2-km simulation discussed below used the triple-moment version of the multimoment bulk scheme described in Milbrandt and Yau (2005a,b) to parameterize cloud microphysical processes at saturated grid points. The scheme partitions the liquid phase into separate categories for cloud "droplets" (diameter <100 μm) and "rain" (diameter >100 μm). Cloud nucleation is based on an assumed "continental-type" aerosol spectrum, which is used to prescribe the initial total number concentration of cloud droplets (N_d) as a function of supersaturation. Visibility is then diagnosed from both the prognostic values of cloud mass content and droplet number concentration using an equation given by Gultepe et al. (2006a). The simulated fields of N_d and LWC are shown in Figs. 15a,b, respectively. The corresponding Vis field is shown in Fig. 15c. The results illustrate that model Vis values can be calculated using the new parameterization. In the future, the CMC will examine the feasibility of applying such techniques for explicit fog forecasting using the operational GEM model.

Vis versus relative humidity. The Vis–RH_w parameterization used in the RUC model (Smirnova et al. 2000) is preset such that Vis reaches 5 km at 95% RH_w. The Vis–RH_w relationship used in the Rapid Update Cycle (RUC) model is shown as the green line in Fig. 16. Using the Vis and RH_w surface observations obtained from Toronto Pearson International Airport, the Vis–RH_w relationship for hourly data for the entire project is also shown in Fig. 16 (black solid line). Then, excluding precipitation, observations from the Alliance Icing Research Study (AIRS2) Mirabel site during the winter of 2003/04 are overlaid on the

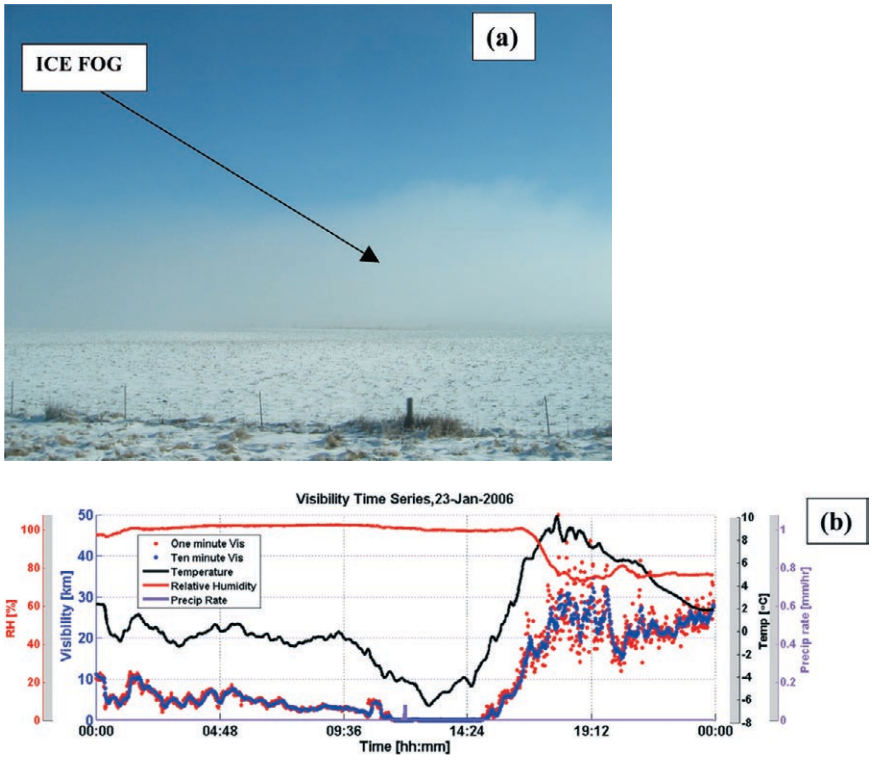

Fig. 13. An example ice fog case: (a) picture taken at 0930 EST on 23 January 2006, and (b) time series of RH_w, visibility averaged over 1-min and 10-min intervals (Vis), temperature (T), and precipitation rate (PR).

plot. A fit to the data is also shown in Fig. 16 (blue line). The results from the FRAM-L observations are shown with percentile lines in red. The relationships for the fits are given in Table 2. Differences between the fits are found to be significant. In general, Vis_{RUC} near 100% RH_w results in about 2 times less than the Vis values obtained from the other datasets. To reduce the climatological effects over which curve should be used for applications, the Vis versus RH_w relationships for FRAM-L with 5%, 50%, and 90% given in Table 2 are suggested. Therefore, the percentile fits and their uncertainties should be used in nowcasting applications.

Frequency distribution of N_d, LWC, and R_{eff}. Accurate statistics of fog LWC, N_d, and R_{eff} are not well known because of a lack of continuous measurements of fog microphysical parameters. Using the FMD instru-

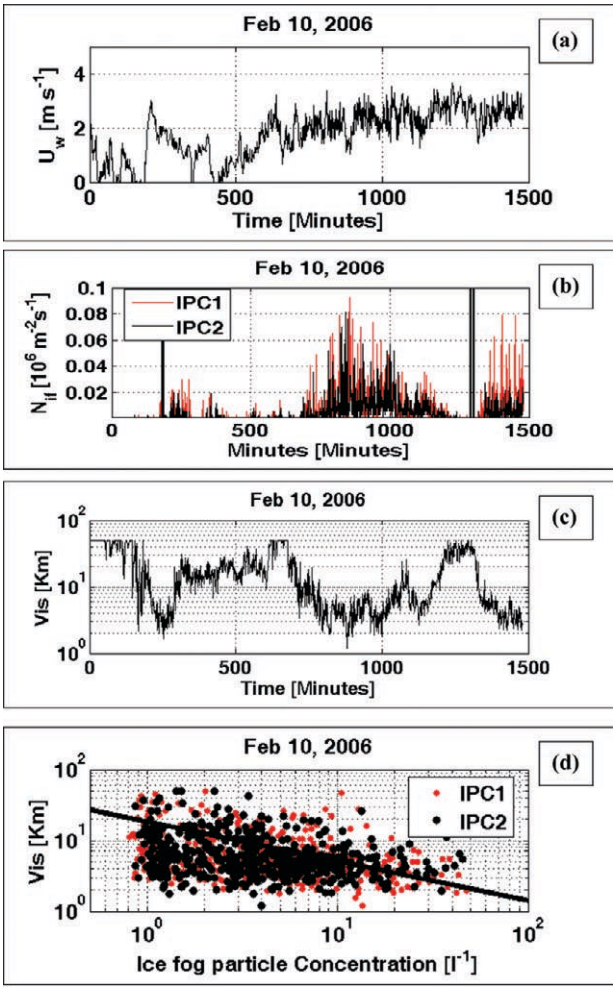

Fig. 14 (above). Time series of (a) horizontal wind speed, (b) ice crystal mass flux, (c) visibility, and (d) visibility versus ice crystal number concentration. The black line is for the eye-fit to the data. Red and black dots represent IPC1 and IPC2, respectively. Both instruments were located at 10 m meteorological tower that included other conventional observations.

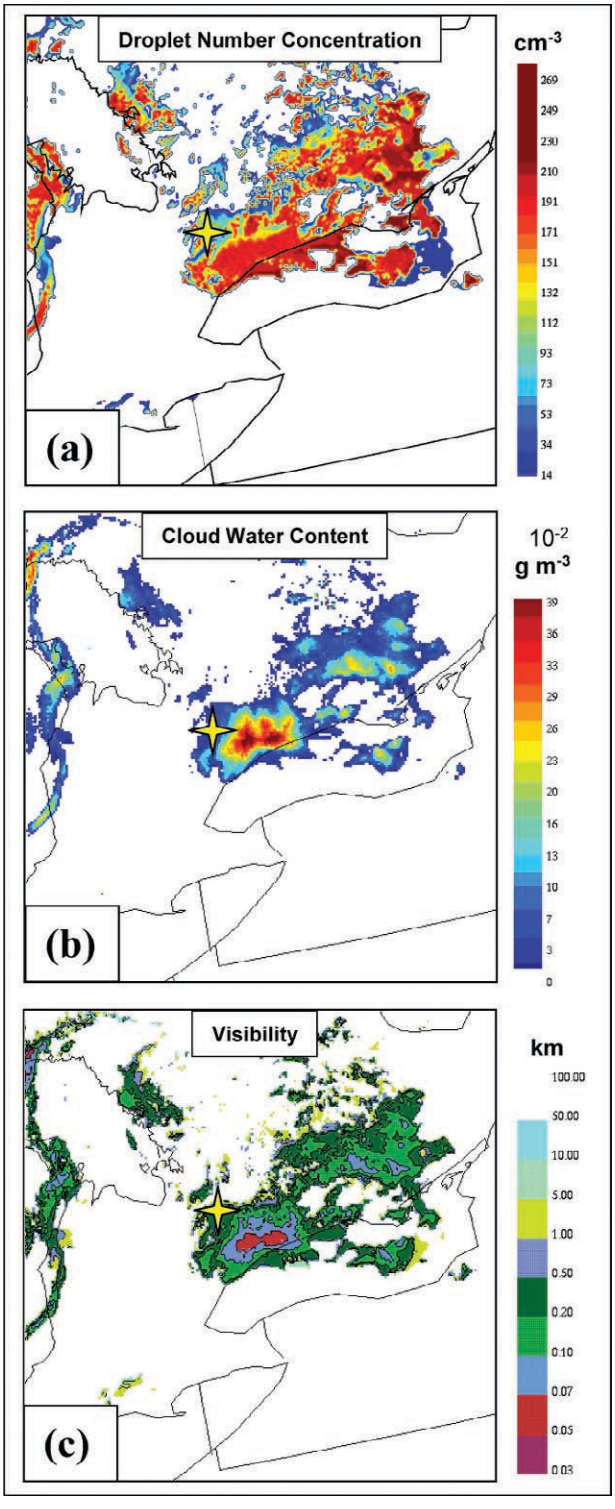

Fig. 15 (right). (a) Droplet number concentration, (b) LWC, and (c) visibility obtained from the MC2 simulations valid at 1600 EST for the 4 Jan 2006. The four-point star with yellow color indicates the FRAM project site.

ment, this deficiency (lack of continuous measurements) can be resolved because of its stable and long-term unattended measurement capability. Knowing the statistics of fog microphysical parameters can help in the evaluation of model products and remote sensing retrievals, thereby leading to better evaluation of fog conditions. Using the observations from the FMD, the frequency and cumulative frequency are shown in Fig. 17 for each microphysical parameter. Some differences between land (FRAM-C) and ocean (FRAM-L) fog cases are seen. The median value of LWC for both FRAM-C and FRAM-L projects are found at about 0.02–0.03 g m^{-3}. The LWC at the 100% cumulative frequency (Figs. 17a,d) corresponds to ~0.3 g m^{-3} for both FRAM-C and FRAM-L. The median values of N_d for the ocean and land fog cases are ~50 and ~90 cm^{-3}, respectively (Figs. 17b,e). These values are within the range of N_d measurements given in Gultepe and Isaac (2004). The R_{eff} was 7–8 μm for both projects, but larger values were obtained during FRAM-L (Figs. 17c,f).

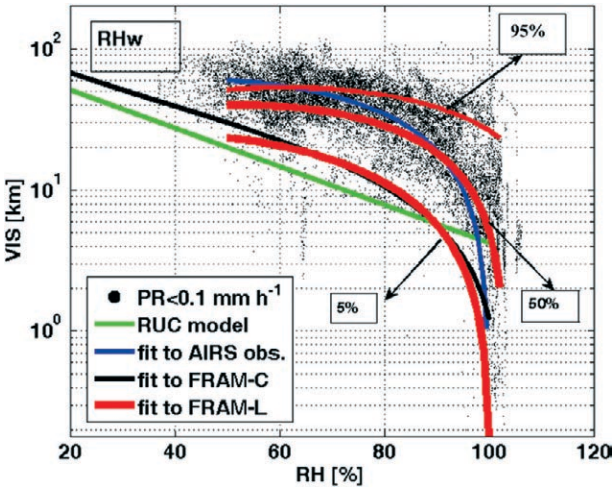

Fig. 16. Visibility (Vis) versus relative humidity with respect to water (RH_w) for AIRS2 measurements (dots), and a fit to the observations (solid blue line). The black solid line is based on hourly observations from the Pearson Airport site. The green line represents the RUC model parameterization. The red lines are for the fits to 5%, 50%, and 95% of the FRAM observations. Note that the fits beyond the limits should be fixed to their end values (see Table 2).

SUMMARY AND CONCLUSIONS. This paper provides an overview of the FRAM project field campaigns. The FRAM field campaigns, which measured both maritime and continental fog conditions, were performed during the winter of 2005/06 and the summers of 2006 and 2007. The objectives of the FRAM project are to better understand the life cycle of maritime and continental fog, improve parameterizations of fog microphysics for modeling and remote sensing applications, and develop better forecasting skills. Only a small part of the dataset has been presented here. The results from this project are expected to advance some of the scientific issues related to prediction of fog and low-visibility conditions. Better forecasting/nowcasting skills can help to reduce financial losses arising from road, air, and marine transportation systems, all of which can be significantly impacted by unpredicted low-visibility conditions.

Detailed surface observations included microphysical measurements such as total number concentration and the size and mass spectra of droplets and aerosols. MODIS- and GOES-based products were archived for future development and evaluation. Although a modeling component was not available during the project, microphysical parameterizations were developed for operational model applications (Gultepe et al. 2006a), and they are now being considered and evaluated for forecasting models. A fog climatology from 1970 to 2004 is being developed for Canadian airports (Hansen et al. 2007; available online at http://collaboration.cmc.ec.gc.ca/science/arma/climatology). The results of FRAM suggested that integration of observations from various instruments (Table 1) and remote sensing platforms together with model outputs can lead to improved understanding of fog processes at various space scales.

Table 2. Vis vs RH_w relationships based on various field programs and from the RUC model.

Parameterizations	Conditions	References
$Vis_{RUC} = 60 \exp(-2.5*(RH_w - 15)/80)$	Set to 5 km at RH_w = 95%	RUC model
$Vis_{FRAM\text{-}C} = -41.5 \ln(RH_w) + 192.3$	For RH_w > 30%	Gultepe et al. (2006)
$Vis_{AIRS} = -0.0177RH_w^2 + 1.462RH_w + 30.8$	For RH_w > 30%	Gultepe et al. (2006)
$Vis_{FRAM\text{-}L(95\%)} = -0.0001143RH_w^{2.6983} + 27.4449$	For RH_w > 30%	FRAM (present work)
$Vis_{FRAM\text{-}L(50\%)} = -5.1906*10^{-10}RH_w^{5.4346} + 40.097$	For RH_w > 30%	FRAM (present work)
$Vis_{FRAM\text{-}L(5\%)} = -9.6768*10^{-14}RH_w^{7.1899} + 52.1981$	For RH_w > 30%	FRAM (present work)

The important conclusions obtained from the present work are given below.

- Fog microphysical characteristics for marine and continental fogs were found to be significantly different, and they require separate parameterizations.
- Remote sensing observations from a cloud radar, profiling microwave radiometer, and satellites can be useful for observation of fog coverage, visibility, and phase.
- Interaction of microphysical, dynamical (e.g., turbulence), radiative processes, and surface conditions (e.g., soil moisture and temperature) can play an important role for the life cycle of fog. This was simulated using a detailed forecast model and observations collected during the FRAM project (Gultepe and Milbrandt 2007).
- Several new instruments were used to collect observations of fog environments, such as the FMD and Vaisala surface-state instruments; these data can be used to validate model simulations. The Vis versus RH_w parameterizations need to be validated because current relationships show large variability.
- A combination of fog and precipitation observations can increase the understanding of the role of light precipitation that presently is not considered in the calculation of the annual precipitation amount.
- Based on incoming SW broadband radiative flux measurements, temperature change resulting from fog effect can reach up to –9°C h^{-1} over a 1-km-thick fog layer.
- Limited occurrence of ice fog during FRAM-C suggests that Vis can be significantly affected by small ice crystals; therefore, it needs to be considered in future studies.
- Gultepe et al. (2007b) show that integration of model-based parameters such as RH_w and T at the surface together with satellite-based algorithms can improve fog forecasting up to 30%.

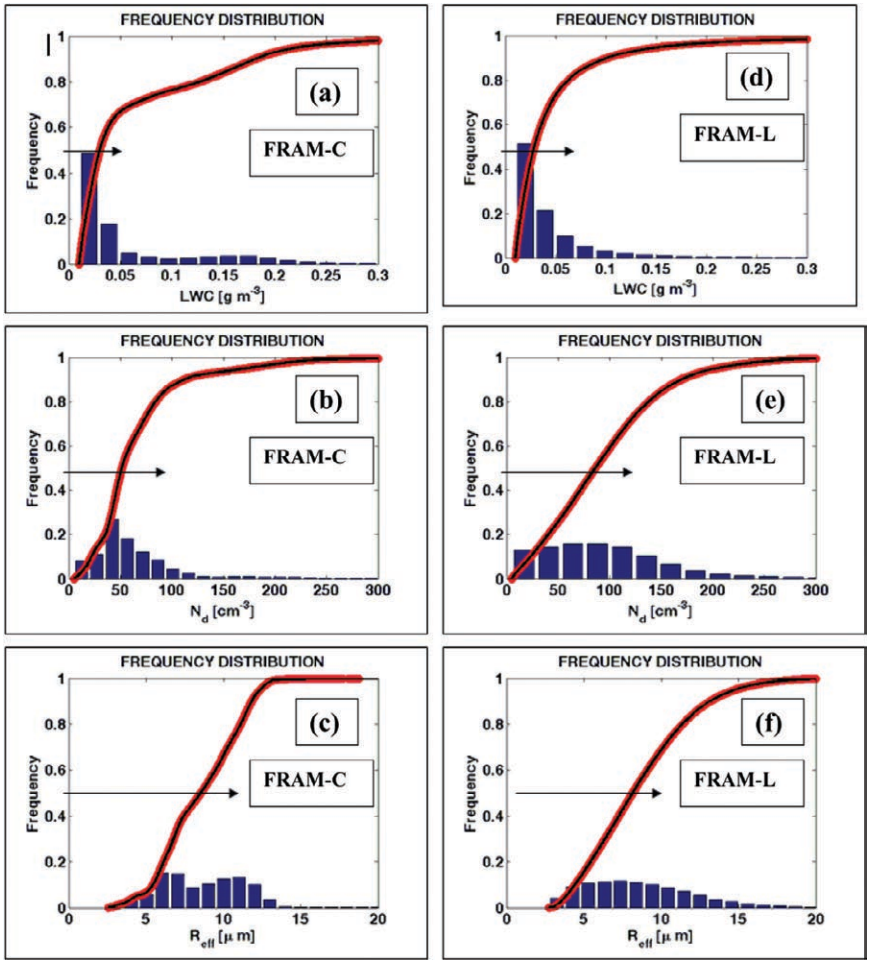

FIG. 17. The histograms and cumulative probability curves for (a) liquid water content (LWC), (b) droplet number concentration (N_d), and (c) effective radius (R_{eff}), for FRAM-C; (d)–(f) similar plots shown for FRAM-L. These plots are obtained with LWC > 0.005 g m^{-3}, N_d > 5 cm^{-3} (to remove the aerosols).

Overall, extensive observations obtained during the FRAM projects will let us describe the marine and continental fog conditions at various temperatures and compare fog microphysics to the results obtained from the numerical simulations and satellite-based analysis. Presently, both the operational and research communities are involved in the analysis of data, and results will be presented in future works.

ACKNOWLEDGMENTS. Funding for this work was provided by the Canadian National Search and Rescue Secretariat and Environment Canada. ISDAC was

supported by the Office of Biological and Environmental Research of the U.S. Department of Energy (Grant No. DE-FG02-08ER64554) through the Atmospheric Radiation Measurement (ARM) program and the ARM Aerial Vehicle Program with contributions from the DOE Atmospheric Sciences Program (ASP), and Environment Canada and the National Research Council of Canada. Data were obtained from the ARM program archive, sponsored by the U.S. DOE, Office of Science, Office of Biological and Environmental Research, Environmental Sciences Division. Some additional funding was also provided by the European COST-722 fog initiative project office. Authors are thankful to G. Isaac for instrumental support, M. Wasey and R. Reed of Environment Canada for technical support, and J. W. Strapp for discussions on the TP3000 MWR during FRAM.

REFERENCES

Bélair, S., L. P. Crevier, J. Mailhot, B. Bilodeau, and Y. Delage, 2003a: Operational implementation of the ISBA land surface scheme in the Canadian regional weather forecast model. Part I: Warm season results. *J. Hydrometeor.,* **4,** 352–370.

——, R. Brown, J. Mailhot, B. Bilodeau, and L. P. Crevier, 2003b: Operational implementation of the ISBA land surface scheme in the Canadian regional weather forecast model. Part II: Cold season results. *J. Hydrometeor.,* **4,** 371–386.

Bendix, J., B. Thies, T. Nauss, and J. Cermak, 2006: A feasibility study of daytime fog and low stratus detection with TERRA/AQUA-MODIS over land. *Meteor. Appl.,* **13,** 111–125.

Benoit, R. J., J. Côté, and J. Mailhot, 1989: Inclusion of a TKE boundary layer parameterization in the Canadian regional finite-element model. *Mon. Wea. Rev.,* **117,** 1726–1750.

——, J. M. Desgagné, P. Pellerin, S. Pellerin, Y. Chartier, and S. Desjardins, 1997: The Canadian MC2: A semi-Lagrangian, semi-implicit wideband atmospheric model suited for finescale process studies and simulation. *Mon. Wea. Rev.,* **125,** 2382–2415.

Bergot, T., D. Carrer, J. Noilhan, and P. Bougeault, 2005: Improved site-specific numerical prediction of fog and low clouds: A feasibility study. *Wea. Forecasting,* **20,** 627–646.

Bott, A., 1991: On the influence of the physico-chemical properties of aerosols on the life cycle of radiation fogs. *Bound.-Layer Meteor.,* **56,** 1–31.

——, U. Sievers, and W. Zdunkowski, 1990: A radiation fog model with a detailed treatment of the interaction between radiative transfer and fog microphysics. *J. Atmos. Sci.,* **47,** 2153–2166.

Bowling, S. A., Ohtake, T., and Benson, C. S., 1968: Winter pressure systems and ice fog in Fairbanks, Alaska. *J. Appl. Meteor.,* **7,** 961–968.

Brown, T., and J. W. Pomeroy, 1989: A blowing snow particle detector. *J. Cold Regions Sci. Technol.,* **16,** 167–174.

Cermak, J., and J. Bendix, 2007: Dynamical nighttime fog/low stratus detection based on Meteosat SEVIRI data—A feasibility study. *J. Pure Appl. Geophys.,* **164,** 1179–1192.

——, and J. Bendix, 2008: A novel approach to fog/low stratus detection using Meteosat 8 data. *Atmos. Res.,* **87,** 279–292.

Chang, F.-L., and Z.-Q. Li, 2003: Retrieving vertical profiles of water-cloud droplet effective radius: Algorithm modification and preliminary application. *J. Geophys. Res.,* **108,** 4762, doi:10.1029/2003JD003906.

Choularton, T. W., G. Fullarton, J. Latham, C. S. Mill, M. H. Smith, and I. M. Stromberg, 1981: A field study of radiation fog in Meppen, West Germany. *Quart. J. Roy. Meteor. Soc.,* **107,** 381–394.

Côté, J., S. Gravel, A. Methot, A. Patoine, M. Roach, and A. Staniforth, 1998: The operational CMC-MRB Global Environmental Multiscale (GEM) model. Part I: Design considerations and formulation. *Mon. Wea. Rev.,* **126,** 1373–1395.

Ellrod, G. P., 1995: Advances in the detection and analysis of fog at night using GOES multispectral infrared imagery. *Wea. Forecasting,* **10,** 606–619.

——, and I. Gultepe, 2007: Inferring low cloud base heights at night for aviation using satellite infrared and surface temperature data. *J. Pure Appl. Geophys.,* **164,** 1193–1205.

Fouquart, Y., and B. Bonnel, 1980: Computations of solar heating of the earth's atmosphere: A new parameterization. *Contrib. Atmos. Phys.,* **53,** 35–62.

Fuzzi, S., and Coauthors, 1992: The Po Valley Fog Experiment 1989: An overview. *Tellus,* **44B,** 448–468.

——, and Coauthors, 1998: Overview of the Po Valley Fog Experiment 1994 (Chemdrop). *Contrib. Atmos. Phys.,* **71,** 3–19.

Gadher, D., and T. Baird, cited 2007: Airport dash as the fog lifts. *The Sunday Times,* posted online 24 December 2006. [Available online at www.timesonline.co.uk/tol/news/uk/article1264290.ece.]

Garand, L., and J. Mailhot, 1990: The influences of infrared radiation on numerical weather forecasts. Preprints, *Seventh Conf. on Atmospheric Radiation,* San Francisco, CA, *Amer. Meteor. Soc.,* J146–151.

Girard, E., and J. P. Blanchet, 2001: Simulation of arctic diamond dust, ice fog, and thin stratus using an explicit aerosol–cloud–radiation model. *J. Atmos. Sci.,* **58,** 1199–1221.

Gordon, M., K. Simon, and P. A. Taylor, 2006: On snow depth predictions with the Canadian land surface scheme including a parameterization of blowing snow sublimation. *Atmos.–Ocean,* **44,** 239–255.

Gotaas, Y., and C. S. Benson, 1965: The effect of suspended ice crystals on radiative cooling. *J. Appl. Meteor.,* **4,** 446–453.

Guedalia, D., and T. Bergot, 1994: Numerical forecasting of radiation fog. Part II: A comparison of model simulation with several observed fog events. *Mon. Wea. Rev.,* **122,** 1231–1246.

Gultepe, I., and G. Isaac, 2004: An analysis of cloud droplet number concentration (N_d) for climate studies: Emphasis on constant N_d. *Quart. J. Roy. Meteor. Soc.,* **130,** 2377–2390.

——, and ——, 2006: Visbility versus precipitation rate and relative humidity. Preprints, *12th Cloud Physics Conf.,* Madison, WI, Amer. Meteor. Soc., P2.55. [Available online at http://ams.confex.com/ams/Madison2006/techprogram/paper_113177.htm.]

——, and J. A. Milbrandt, 2007: Microphysical observations and mesoscale model simulation of a warm fog case during FRAM project. *J. Pure Appl. Geophys.,* **164,** 1161–1178.

——, G. A. Isaac, and S. G. Cober, 2001: Ice crystal number concentration versus temperature for climate studies. *Int. J. Climatol.,* **21,** 1281–1302.

——, M. D. Müller, and Z. Boybeyi, 2006a: A new visibility parameterization for warm fog applications in numerical weather prediction models. *J. Appl. Meteor.,* **45,** 1469–1480.

——, S. G. Cober, P. King, G. Isaac, P. Taylor, and B. Hansen, 2006b: The Fog Remote Sensing and Modeling (FRAM) field project and preliminary results. Preprints, *12th Cloud Physics Conf.,* Madison, WI, 4.3. [Available online at http://ams.confex.com/ams/Madison2006/techprogram/paper_113412.htm.]

——, and Coauthors, 2007a: Fog research: A review of past achievements and future perspectives. *J. Pure Appl. Geophys.,* **164,** 1121–1159.

——, M. Pagowski, and J. Reid, 2007b: Using surface data to validate a satellite-based fog detection scheme. *Wea. Forecasting,* **22,** 444–456.

——, J. Milbrandt, S. Benjamin, G. A. Isaac, S. G. Cober, C. Flynn, and B. Hansen, 2008: Visibility parameterizations for forecasting applications. *Int. Conf. on Clouds and Precipitation (ICCP),* Cancun, Mexico, 13.9, 11 pp.

Hamazu, K., H. Hashiguchi, T. Wakayama, T. Matsuda, R. J. Doviak, and S. Fukao, 2003: A 35-GHz scanning Doppler radar for fog observations. *J. Atmos. Oceanic Technol.,* **20,** 972–986.

Hansen, B., I. Gultepe, P. King, G. Toth, and C. Mooney, 2007: Visualization of seasonal-diurnal climatology of visibility in fog and precipitation at Canadian airports. Preprints, *16th Conf. on Applied Climatology,* San Antonio, TX, Amer. Meteor. Soc., P1.3. [Available online at http://ams.confex.com/ams/87ANNUAL/techprogram/paper_117973.htm.]

Huang, Q., J. Hanesiak, S. Savelyev, T. Papakyriakou, and P. A. Taylor, 2007: Visibility during blowing snow events over arctic sea ice. *Wea. Forecasting,* **23,** 741–751.

Jacobs, W., V. Nietosvaara, A. Bott, J. Bendix, J. Cermak, M. Silas, and I. Gultepe, 2007: Short range forecasting methods of fog visibility and low clouds. Earth System Science and Environmental Management Final Rep. on COST-722 Action, 489 pp. [Available from COST Office, Avenue Louise 149, B-1050 Brussel, Belgium.]

Kloesel, K. A., 1992: A 70-year history of marine stratocumulus cloud field experiments off the coast of California. *Bull. Amer. Meteor. Soc.,* **73,** 1581–1585.

Koracin, D., J. Lewis, W. T. Thompson, C. E. Dorman, and J. A. Businger, 2001: Transition of stratus into fog along the California coast: Observations and modeling, *J. Atmos. Sci.,* **58,** 1714–1731.

Kunkel, B. A., 1984: Parameterization of droplet terminal velocity and extinction coefficient in fog models. *J. Climate Appl. Meteor.,* **23,** 34–41.

Leipper, D. F., 1994: Fog on the U.S. west coast: A review. *Bull. Amer. Meteor. Soc.,* **75,** 229–240.

Mailhot, J., S. Bélair, R. Benoit, B. Bilodeau, Y. Delage, L. Fillion, L. Garand, C. Cirard, and A. Tremblay, 1998: Scientific description of RPN physics library—Version 3.6. Recherche en prévision numérique, 188 pp. [Available online at http://collaboration.cmc.ec.gc.ca/science/rpn/physics/physics98.pdf.]

Mead, J. B., R. E. Mcintosh, D. Vandemark, and C. T. Swift, 1989: Remote sensing of clouds and fog with a 1.4-mm radar. *J. Atmos. Oceanic Technol.,* **6,** 1090–1097.

Meyer, M. B., and G. G. Lala, 1986: FOG-82: A cooperative field study of radiation fog. *Bull. Amer. Meteor. Soc.,* **65,** 825–832.

Milbrandt, J. A., and M. K. Yau, 2005a: A multimoment bulk microphysics parameterization. Part I: Analysis of the role of the spectral shape parameter. *J. Atmos. Sci.,* **62,** 3051–3064.

——, and M. K. Yau, 2005b: A multimoment bulk microphysics parameterization. Part II: A proposed three-moment closure and scheme description. *J. Atmos. Sci.,* **62,** 3065–3081.

Milmo, D., 2007: BAA counts the cost of December fog. *Guardian Unlimited,* posted 9 January 2007. [Avail-

able online at www.guardian.co.uk/business/2007/jan/09/theairlineindustry.travel.]

Müller, M. D., C. Schmutz, and E. Parlow, 2007: A one-dimensional ensemble forecast and assimilation system for fog prediction. *J. Pure Appl. Geophys.,* **164,** (Special issue), 1241–1264.

Noonkester, V. R., 1977: Marine fog investigation at San Diego during CEWCOM-1976. Naval Ocean Systems Center Tech. Rep. 172, 77 pp.

Oakley, J. P., and B. Satherley, 1998: Improving image quality in poor visibility conditions using a physical model for contrast degradation. *IEEE Trans. Image Process.,* **7,** 167–179.

Ohtake, T., and P. J. Huffman, 1969: Visual range in ice fog. *J. Appl. Meteor.,* **8,** 499–501.

Pagowski, M., I. Gultepe, and P. King, 2004: Analysis and modeling of an extremely dense fog event in southern Ontario. *J. Appl. Meteor.,* **43,** 3–16.

Petterssen, J., 1956: *Weather Analysis and Forecasting.* 2nd ed. McGraw-Hill, 266 pp.

Platnick, S., 2000: Vertical photon transport in cloud remote sensing problems. *J. Geophys. Res.,* **105,** 22 919–22 935.

——, M. D. King, S. A. Ackerman, W. P. Menzel, B. A. Baum, J. C. Riedi, and R. A. Frey, 2003: The MODIS cloud products: Algorithms and examples from Terra. *IEEE Trans. Geosci. Remote Sens.,* **41,** 459–473.

Roach, W., R. Brown, S. J. Caughey, J. A. Garland, and C. J. Readings, 1976: The physics of radiation fog: I-A field study. *Quart. J. Roy. Meteor. Soc.,* **102,** 313–333.

Savelyev, S. A., M. Gordon, J. Hanesiak, T. Papakourioki, and P. A. Taylor, 2006: Blowing snow studies in CASES Canadian Arctic Shelf Exchange Study (CASES). *Hydrol. Process.,* **4,** 817–827.

Smirnova, T. G., S. G. Benjamin, and J. M. Brown, 2000: Case study verification of RUC/MAPS fog and visibility forecasts. Preprints, *Ninth Conf. on Aviation, Range, and Aerospace Meteorology,* Orlando, FL, Amer. Meteor. Soc., P2.3.

Stoelinga, M. T., and T. T. Warner, 1999: Nonhydrostatic, Mesobeta-scale model simulations of cloud ceiling and visibility for an East Coast winter precipitation event. *J. Appl. Meteor.,* **38,** 385–404.

Sundqvist, H., E. Berge, J. E. Kristjansson, 1989: Condensation and cloud parameterization studies with a mesoscale numerical weather prediction model. *Mon. Wea. Rev.,* **117,** 1641–1657.

Tardif, R., 2007: The impact of vertical resolution in the explicit numerical forecasting of radiation fog: A case study. *J. Pure Appl. Geophys.,* **164** (Special issue), 1221–1240.

——, and R. M. Rasmussen, 2007: Event-based climatology and typology of fog in the New York City region. *J. Appl. Meteor.,* **46,** 1141–1168.

Teixeira, J., 1999: Simulation of fog with the ECMWF prognostic cloud scheme. *Quart. J. Roy. Meteor. Soc.,* **125,** 529–553.

Thomas, S. J., C. Girard, R. Benoit, M. Desgagne, and P. Pellerin, 1998: A new adiabatic kernel for the MC2 model. *Atmos.–Ocean,* **36,** 241–270.

Transport Canada, 2001: Trends in motor vehicle traffic collision statistics 1988–1997. Transport Canada Tech. Rep. TP 13743 E, 155 pp.

Uematsu, A., H. Hashiguchi, M. Teshiba, H. Tanaka, K. Hirashima, and S. Fukao, 2005: Moving cellular structure of fog echoes obtained with a millimeter-wave scanning Doppler radar at Kushiro, Japan. *J. Appl. Meteor.,* **44,** 1260–1273.

Westcott, N. E., 2007: Some aspects of dense fog in the Midwestern United States. *Wea. Forecasting,* **22,** 457–465.

Wolf, D. A., C. Kontogeorgakis, and R. E. Marshall, 1999: Reflectivity and attenuation at millimeter to infrared wavelength for advection fogs at four locations. *J. Appl. Meteor.,* **38,** 126–131.